THE DISTRIBUTION AND ORIGIN OF MERCURY'S LITHOSPHERIC MAGNETIZATION. Catherine L. Johnson[1,2], Alain M. Plattner[3], Roger J. Phillips[4], Lydia C. Philpott[1], Mallory Kinczyk[5] and Louise Prockter[6], [1]Dept.of Earth, Ocean and Atmospheric Sciences, University of British Columbia, Vancouver, BC, V6T 1Z4, Canada, cjohnson@eoas.ubc.ca. [2]Planetary Science Institute, Tucson, AZ 85719, USA, cjohnson@psi.edu. [3] Dept. of Earth and Environmental Sciences, California State University, Fresno, CA 93740, USA. [4]Dept. of Earth and Planetary Sciences, Washington University, St Louis, MO 63130, USA. [5]Dept. of Marine, Earth, and Atmospheric Sciences, North Carolina State University, Raleigh, NC, 27695, USA. [6]Lunar and Planetary Institute, Houston, TX 77058, USA.

Overview: Magnetic field data obtained by the MErcury Surface, Space ENvironment, GEochemistry, and Ranging (MESSENGER) spacecraft have been used to demonstrate the presence of lithospheric magnetization on Mercury [1]. Initial regional lithospheric field models have been obtained covering restricted [2,3], and all [4] northern hemisphere longitudes. Here we derive and present models for Mercury's lithospheric magnetization and the associated magnetic field using the complete low-altitude magnetic field data set returned by MESSENGER. We compute uncertainty estimates for the models to place bounds on the minimum and maximum magnetizations permitted by the observations. The strongest magnetizations and magnetic fields are spatially associated with the Caloris and circum-Caloris regions, and are sometimes, but not always, associated with impact basin interiors and/or ejecta materials. Elsewhere, magnetization and magnetic field amplitudes are typically weaker and exhibit shorter coherence length scales, including over the northern smooth plains. We discuss the relative contributions of induced versus remanent magnetization, and place constraints on the depth distribution of magnetization.

Modeling Approach: Magnetic fields measured at MESSENGER spacecraft altitudes are dominated by fields from sources other than lithospheric magnetization (Fig 1a,b). After removal of these fields, the residual signals were inverted to obtain models for the spatial distribution of magnetization and the associated lithospheric magnetic field.

Isolating the Lithospheric Magnetic Field. Data from anomalous orbits (e.g., during coronal mass ejections) were excluded. Fields resulting from the core dynamo and the magnetospheric current systems were estimated using the magnetospheric model of [5,6] and subtracted from the magnetic field data. The resulting fields are still dominated by fields from Birkeland currents [7] that vary substantially in amplitude and wavelength on an orbit-to-orbit basis (Fig. 1b). These were estimated and subtracted using two distinct empirical approaches to isolate lithospheric signals with wavelengths less than ~700 km. In the first approach, an along-track high-pass filter (HPF) was applied on an orbit-by-orbit basis (see [1] for details). In a second approach, a 2D (i.e. both along- and across-track) representation of the full vector field that describes the field due to the Birkeland currents was determined using vector Slepian functions [8]. Because the vector Slepian filtering (VSF) was not tuned to individual orbits it yielded somewhat noisier residual signals (Fig. 1d), especially at latitudes above 70°N where the Birkeland currents dominate. Importantly though, the VSF confirms the overall structure in the residuals obtained from along-track filtering (Fig. 1c).

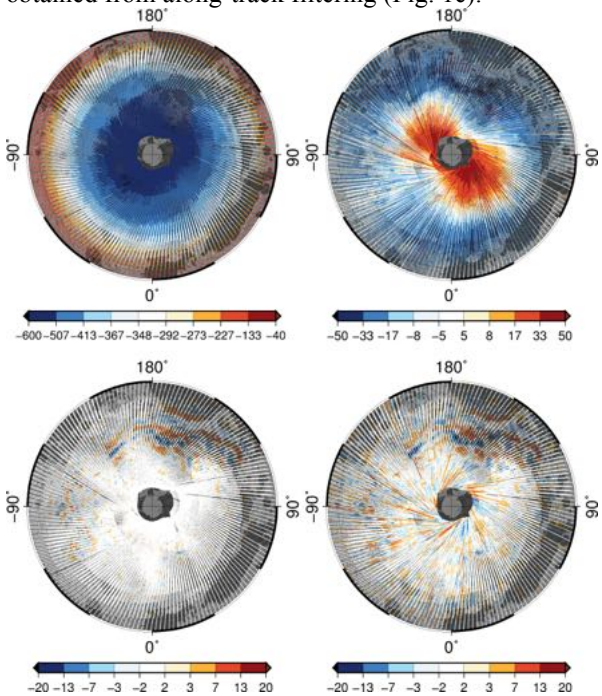

Figure 1. (a) Radial component of the magnetic field, B_r, measured at MESSENGER spacecraft altitudes below 120 km. Lambert azimuthal equal area projection in the body-fixed frame from 35° to 90° N. (b) B_r after subtraction of the offset axial dipole field and the magnetopause and magnetotail fields predicted by [5,6]. (c) B_r after HPF of the signals in Fig. 1b [1], retaining signals with wavelengths less than ~700 km and local times between 1600 and 0800. (d) B_r after VSF of the signals in Fig. 1b. Local times as in Fig. 1c. Background image shows smooth plains (dark gray) and intercrater plains (light gray) [9]. All scale bars in nT. Note the small amplitude of crustal fields.

Magnetization Models. We inverted for magnetization distributions using an equivalent source dipole (ESD) technique [10]. In a bootstrap fashion, we sub-

sampled the HPF (or VSF) data with respect to their altitude and along-track vs. across-track spacing to obtain a hundred 'modeling' data subsets together with their complementing 'evaluation' subsets, each with a more equal-area-distribution. Each of these hundred modeling subsets were inverted using a classical regularized inversion approach [11]. The averaged trade-off curves computed for the evaluation subsets exhibit a clear minimum in misfit – *i.e.,* at some point the increased model structure warranted by data used in the inversion is incompatible with the rest of the data. We averaged the models from this iteration in the inversion (Fig. 2, left). The approach has two additional benefits: a model uncertainty could be computed (Fig. 2, right) and a dipole spacing less than the cross-track spacing could be used because dipole moments poorly resolved by the data distribution have large associated uncertainties. Our inversions used a single equivalent source layer and a dipole spacing of ~27 km.

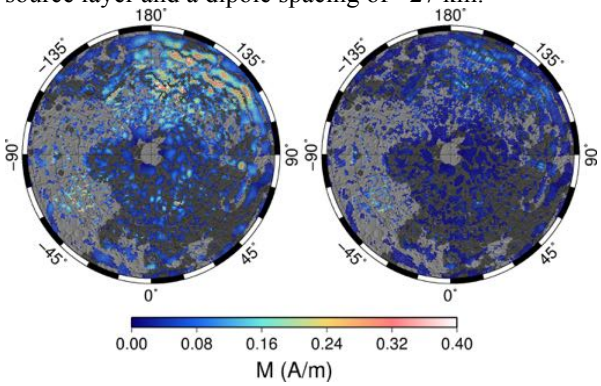

Figure 2. Magnetization model (left) and model uncertainty (right) obtained from ESD inversions of the HPF data in Fig. 1c. Magnetizations and their uncertainty are shown where they are significantly different from zero at the 1-sigma level. Magnetizations, *M*, were computed assuming a 10-km thick magnetized layer. Lambert azimuthal equal area projection from 38° to 90° N.

Lithospheric Magnetic Fields. The magnetization model was used to predict the surface magnetic field and its uncertainty (Fig. 3). In a second independent approach we computed the surface field directly form the HPF or VSF data using altitude-cognizant gradient vector Slepian functions ([12], not shown here).

Discussion: The magnetization model and associated surface fields show largest amplitudes in association with the Caloris region. Furthermore, in this region, the amplitudes associated with the smooth plains are consistently larger. This is in contrast to elsewhere in the northern hemisphere where cumulative distribution functions show weak magnetizations associated with both intercrater plains and smooth plains. No correlation of magnetization with crustal thickness is observed. Individual instances of correlations of magnetization with crater interiors and ejecta materials are seen (e.g., Rustaveli crater at ~83°E, 52°N, Fig. 2), however no global systematic trends with crater location or degradation state [13] have been observed.

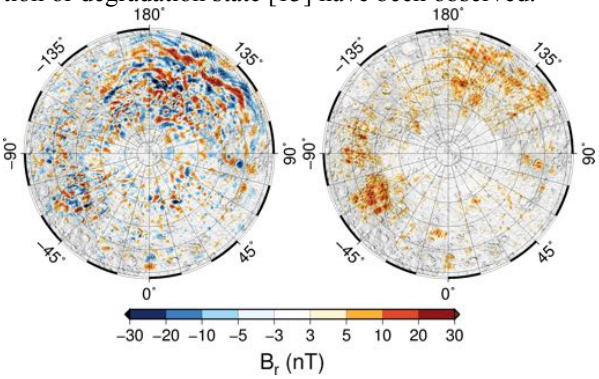

Figure 3. Surface radial magnetic field (left) and model uncertainty (right) predicted by the magnetization model in Fig. 2. Underlying image is shaded relief derived from the Mercury Laser Altimeter.

Magnetization source depths are constrained by observations along individual orbits at the lowest altitudes, along-track spectra and the spectral slope of regional spherical harmonic models. Collectively, these suggest that source depths for most signals are a few km to ~40 km depth, typically within the crust.

The average magnetization model, together with low-field susceptibilities appropriate for likely magnetic mineralogies on Mercury [1] demonstrate that induced magnetizations may contribute some, but not all, of the measured lithospheric signal. However, the lower 95% bound on magnetization inferred from our models, together with the upper 95% confidence limit on low-field susceptibilities permit a scenario in which almost all of the magnetization could be induced in the present field. Further constraints on the properties of possible magnetic mineralogies at Mercury [14] are needed as this is a critically important issue to resolve for understanding Mercury's thermal history.

References: [1] Johnson, C. L. et al. (2015) *Science*, 348, 892. [2] Hood, L. L. (2015) *GRL*, 42, 10,565. [3] Hood, L. L. (2016) *JGR Planets,* 121, 1016. [4] Johnson et al. (2016) *LPS XXXXVII,* Abstract #1391. [5] H. Korth et al. (2015) *JGR Space Physics*, 120, 4503. [6] H. Korth et al. (2017) *GRL*, 44, 10,147. [7] Anderson, B. J. et al. (2014) *GRL*, 41, 7444. [8] Plattner, A. and F. J. Simons (2014) *Appl. Comput. Harmon. Anal.* 36, 1. [9] B. W. Denevi et al. (2013) *JGR Planets*, 118, 891. [10] B. Langlais et al. (2004) *JGR*, 109, E02008. [11] R. C. Aster et al. (2013) *Parameter Estimation and Inverse Problems*, 2nd ed., Academic Press. [12] Plattner, A. and F. J. Simons (2017), *Geophys. J. Int.*, 211, 207. [13] Kinczyk, M. et al. (2016) *LPS XXXVII*, Abstract #1573. [14] Strauss, B. et al. (2016), *JGR Planets*, 121, 2225.